RSC Advances

ROYAL SOCIETY OF CHEMISTRY

PAPER

View Article Online
View Journal | View Issue

Cite this: *RSC Adv.*, 2024, **14**, 7699

A rapid supercritical water approach for one-pot synthesis of a branched $BiVO_4$/RGO composite as a Li-ion battery anode

Dinesh Rangappa,†[a] Karnan Manickavasakam,†[b] Murthy Muniyappa,[c] Chandrakantha Bekal,[d] Satish Shenoy B,[d] Izan Izwan Misnon,[bg] Manikandan Kandasamy[ef] and Manjunath Shetty*[d]

The application of novel one-dimensional (1D) architectures in the field of energy storage has fascinated researchers for a long time. The fast-paced technological advancements require reliable rapid synthesis techniques for the development of various Multi-metal oxide (MMO) nanostructures. For the first time, we report the synthesis of a single-phase hierarchical one-dimensional (1D) branched $BiVO_4$-Reduced Graphene Oxide (BVONB/RGO) nanocomposite with different weight percent variations of RGO starting from 6, 12, 24, and 26 wt% using the supercritical water method (SCW). The affirmation of the sample characteristics is done through various nano-characterization tools that help in establishing the monoclinic crystal structure, and nano branch morphology along with its physical, and thermal characteristics. Further, the electrochemical behavior evaluations of the fabricated coin cells provide insights into the well-known superior initial cycle capacity of around 810 mA h g^{-1}, showing the superior ability of BVONB structures in storing lithium-ions (Li-ions). Meanwhile, an improved cyclic performance of the pure BVONB/RGO with 260 mA h g^{-1} is evident after 50 cycles. Finally, the reported rapid single-pot SCW approach has delivered promising results in establishing a material process technique for multimetal oxides and their RGO nanocomposites successfully.

Received 12th November 2023
Accepted 29th February 2024

DOI: 10.1039/d3ra07731d

rsc.li/rsc-advances

Introduction

Nanomaterial-based energy storage devices have paved the way for various applications in human life. Specifically, batteries and supercapacitors have reframed the world we live in. Powering a wide range of devices from smartphones to electric vehicles, lithium-ion (Li-ion) batteries and supercapacitors have become an integral part of our daily lives.[1,2] In recent years, to meet the increasing demand for high-performance, long-life, and cost-effective energy storage solutions, there has been a growing interest in the development of new and improved lithium-ion battery and supercapacitor technologies.[3,4] To cater to this need, the research community is consistently dedicating efforts to designing and developing various types of electrode materials.[5] Particularly for the anode, the most commonly used material in Li-ion batteries is graphite, with a theoretical capacity of 372 mA h g^{-1}. However, due to its low lithium insertion voltage and irreversible capacity loss during cycling, the practical capacity of graphite is limited to around 370 mA h g^{-1} (ref. 6) or less. Further exploration for alternative anode materials having higher theoretical capacities and longer cycle life has led to the usage of other anode materials like Lithium and metal oxides. But they also come with limitations such as dendrite formation in Li metal which led to safety concerns despite having the highest theoretical capacity of 3860 mA h g^{-1} (ref. 7) and volume expansion in metal oxide-based anodes, though most of them have a theoretical capacity in the range of 800–200 mA h g^{-1}, which is more than twice higher than graphite.[8] This volume expansion during lithium insertion can lead to mechanical stress, and cracking of the anode, resulting in a rapid capacity fade.[9] To overcome these limitations, researchers have been developing alternate carbon-based conductive electrodes in search of storage performances.[10] But, graphene-based composite anodes that can

[a]*Department of Applied Sciences and Visveswaraya Centre for Nanoscience and Technology, Visveswaraya Technological University, PG Centre Bangalore Region, Muddenahalli, Chikkaballapura 562103, India*

[b]*Center for Advanced Intelligent Materials, Universiti Malaysia Pahang, Kuantan, Pahang, Malaysia*

[c]*Department of Electronics and Communications, Nagarjuna College of Engineering and Technology, Devanahalli, Bengaluru, 562110, Karnataka, India*

[d]*Department of Aeronautical and Automobile Engineering, Manipal Institute of Technology, Manipal Academy of Higher Education (MAHE), Manipal 576104, Karnataka, India. E-mail: manjunath.shetty@manipal.edu*

[e]*Department of Physics, Karpagam Academy of Higher Education, Coimbatore 641021, Tamil Nadu, India*

[f]*Centre for Computational Physics, Karpagam Academy of Higher Education, Coimbatore 641021, Tamil Nadu, India*

[g]*Faculty of Industrial Sciences and Technology, Universiti Malaysia Pahang, Kuantan, Pahang, Malaysia*

† These authors contributed equally.

accommodate volume expansion and exhibit higher theoretical capacity are of prime interest.[11] Graphene with high electronic conductivity and mechanical strength, will certainly improve the rate performance and cycling stability of the existing battery materials.[12] Moreover, graphene-based anodes have a high theoretical capacity and their performance can be improved by combining with high-capacity metal oxides such as V_2O_5,[13] MoO_2,[14] Fe_3O_4,[15] TiO_2,[16] NiO,[17] and Co_3O_4 (ref. 18) are investigated for negative electrodes in LIBs.

Further, metal oxide materials based on bismuth have been investigated as alternative anode materials for lithium-ion batteries.[19] Specifically, bismuth-based nanostructures such as bismuth vanadate ($BiVO_4$),[20] bismuth molybdate (Bi_2MoO_6),[21,22] and bismuth tungstate (Bi_2WO_6)[22] have attracted attention as potential anode materials for Li-ion batteries. These materials possess a theoretical capacity significantly higher than traditional anode materials such as graphite with theoretical capacities of up to 1200 mA h g^{-1}.[23]

Among the above-mentioned bismuth-based nanostructures, $BiVO_4$ is a promising candidate as the electrode for use in Li-ion battery anode due to its high theoretical capacity and improvable stability.[24] Further, various morphologies are being explored but 1D nanostructures are of significant interest owing to their channelized movements of electrons and ions.[25]

To understand the potential of $BiVO_4$ as a potential electrode in lithium-ion batteries further research is needed to fully realize its capabilities. $BiVO_4$ with VO_4 tetrahedron and the BiO_8 dodecahedron form a monoclinic unit cell. The formation of this structure includes the eight oxygen atoms bound to the Bi site, forming a BiO_8 dodecahedron, and four oxygen atoms bound to the V site, forming a VO_4 tetrahedron. The BiO_8 dodecahedron shares an edge with neighbouring BiO_8 dodecahedrons. However, each VO_4 tetrahedron is separate and does not touch any neighbouring VO_4 tetrahedron. The isolated VO_4 tetrahedron is connected to the BiO_8 dodecahedron through the sharing of a vertex oxygen atom. The lithiation, and de-lithiation of lithium ions within the structure of $BiVO_4$ determine the ability to store Li-ions.[26] There are fewer reports evaluating the same, to mention some, Dubal *et al.* studied fern architectures of BVO synthesized using a hydrothermal route. The BVO fern architecture sample provided stable capacities up to 769 mA h g^{-1} at 0.12 A g^{-1}.[24] Furthermore, Dubal *et al.* also evaluated the ability of BVO nanorods as li-ion capacitors, which yielded a reversible specific capacity of 877 mA h g^{-1} at 1.1 A g^{-1}.[27] In other reports, Xie *et al.* synthesized Nd:BVO nanocrystals and employed them for electrodes of li-ion which provided a stable capacity of 611 mA h g^{-1} at 100 mA g^{-1}.[28] Deepak R. Patil synthesized granular BVO to be used as anodes in Li-ion secondary batteries. The hydrothermally grown BVO microspheres in 1% Triton-X structure-directing solution reported a high capacity of 590 mA h g^{-1} at 0.1C.[29] However, similar to all metal oxide-based nanostructures the major challenge allied with $BiVO_4$ nanoparticles is their poor conductivity, which can hinder the performance in storing Li-ions for long cycles.[23] Composites of BVO with conductive additives can be a solution to this limitation. For example, recently, Fang *et al.* synthesized BVO nanowires by an *in situ* coating of polypyrrole using a hydrothermal procedure. The polypyrrole-coated BVO provided a stable discharge capacity of up to 75 mA h g^{-1} for over 50 cycles at 100 mA h g^{-1}.[30] However, reports focused on the characterization and understanding of the effect of RGO on the performance of $BiVO_4$/RGO composite structure is rarely found.

The fundamental focus in the realm of material chemistry has consistently revolved around the connection between a material's structure and its properties. Yet, as far as our knowledge extends, there has been no documented instance of synthesizing BVONB/RGO using supercritical water (SCW) as a solvent. Both supercritical water (SCW) and hydrothermal processes try to utilize the properties of water below and above its critical points that are advantageous in the production of inorganic nanoparticles. In the hydrothermal method, the subcritical temperature and pressure of water are used which is below 374 °C and 22.1 MPa and generally are about 100 to 200 °C at autogenous pressures. Under these conditions, metal salts form metal hydroxides by precipitation. The hydrothermal process is typically carried out from 3 to 24 hours. Contrarily, in the SCW process, the working temperature and pressure are above the critical point. The utilization of water in a supercritical state offers a unique avenue to manipulate reaction kinetics and equilibrium by adjusting solvent density and dielectric constant through variations in temperature and pressure. Thus, supercritical water with its greater diffusivity can be expected to provide higher reaction rates and a smaller size of particles at comparatively low reaction temperature and short reaction time. At a supercritical state, the metal salt solution is elevated to high temperatures and pressures, and extremely high supersaturation is achieved. This offers the advantage of achieving accelerated reaction rates and smaller particle sizes. Within the SCW framework, several key attributes have been identified, namely, the ability to (i) regulate particle size, (ii) influence particle morphology by adjusting temperature and/or pressure, and (iii) create uniform reaction environments for both reduction and oxidation, which can be further enhanced by introducing gases or additional components such as O_2, H_2, or H_2O_2.[31]

Considering the fast, reliable, scalable, and cost-cutting approach for the synthesis of nanoparticles is of paramount importance in moving forward with commercializing nanomaterials for energy storage applications. Per our knowledge, for the first time, the SCW method for synthesizing bismuth vanadate nano branches/RGO (BVONB/RGO) nanocomposite is successfully synthesized by a rapid one-pot approach, and its characterization is being reported. The synthesized BVONB/RGO nanocomposites were examined as Li-ion battery anodes.

Experimental methods and materials

Preparation of BVONB/RGO nanocomposite

To begin with, graphene oxide (GO) was produced using a modified Hummer's technique as reported elsewhere.[32] Further, in a typical experiment, 0.8 ml of HNO_3 was added to 10 ml of DI water. A 1.2 mmol $Bi(NO_3)_3 \cdot 5H_2O$ was dissolved in a mixture of 5 ml of prepared solvent. Further, 1.2 mmol NH_4VO_3 was added to

the other 5 ml mixture of prepared solvent. The prepared solution of $Bi(NO_3)_3 \cdot 5H_2O$ was added to 5 ml of NH_4VO_3 solution and stirred for 30 min to prepare the precursor solution as depicted in Fig. 1. To this, the synthesized GO is added solution mixture of desired weights GO was added and stirred well, further ultrasonicated for 30 min. The above precursor mixture is transferred to a supercritical reactor. The solution was transferred to stainless steel supercritical reactors sealed and the charge was loaded into a furnace preheated to a temperature of 400 °C and the reaction was carried out for 15 minutes. Samples containing Bi : GO weight ratios 0 : 1 (BVONB),1 : 6 (BVONB/RGO-6), 1 : 12 (BVONB/RGO-12), and 1 : 24 (BVONB/RGO-24) were synthesized. Additionally, the same experiment was repeated without GO using different reaction times (5, 10, 15, and 30 min) under identical reaction conditions and the reaction was carried out for 15 min. After the reaction, the autoclave was cooled by quenching in an ice bath to room temperature, after which samples were collected and dried at 70 °C overnight.

Characterization

The crystalline structures of both the BVONB and BVONB/RGO nanocomposite were analyzed using a Rigaku Ultima IV XRD with a wavelength of 0.15406 nm derived from copper radiation, operating at 30 mA and 40 kV across a span of 10° to 70°. The Hitachi SU1510 SEM was employed to scrutinize the morphology and EDS data of the samples. The size and architecture of the nanoparticles were further investigated with a Hitachi H7650 TEM. Raman Spectra, spanning 500–2500 cm^{-1}, were recorded using the Xplora Horiba Scientific. The Xanes Probe II XPS was used, equipped with an Mg K anode, to undertake a qualitative analysis of elemental constituents present on the BVONB/RGO surface. For recognizing the surface functional groups, a range of 400 to 4000 cm^{-1} was chosen and measured using a PerkinElmer FTIR. Lastly, the PerkinElmer STA 8000 performed thermogravimetric analysis at a heating rate of 10 °C min^{-1} in a nitrogen setting. Differential thermal analysis (TGA-DTA) was conducted to ascertain the RGO percentage within the BVONB/RGO nanocomposite.

Electrochemical measurements

The electrochemical measurements were performed using CR2032 coin cells assembled from the synthesized nanoparticles against Li-metal. BVONB and BVONB/RGO nanocomposites were used as active materials (80 wt% of total weight), acetylene black (10 wt%, a conductive mixture), and polyvinylidene fluoride (PVDF, 10 wt%, as a binder), with an organic solvent *N*-methyl pyrrolidone (NMP) for preparation of slurry. The mixture was ground for up to 45 minutes using a mortar and pestle. This resulted in the slurry that was then coated on copper collector foil and dried for 12 h at 90 °C under vacuum conditions. The coated electrode is then punched and dried resulting in the anodes that were later used in the fabrication of the coin cell. The assembly of the half-cell was carried out in argon filled with an EMBRAUN-make glove box. During assembly, the glove box was ensured to have contained very low oxygen and moisture content of less than 0.5 ppm. To fabricate the cell, the coated electrode was combined with a Celgard polypropylene membrane as a separator and a foil of lithium as the counter electrode. The $LiPF_6$ electrolyte was used with ethylene carbonate (EC) and diethyl carbonate (DEC) (DEC : EC = 1 : 1 v/v). A multichannel battery test system of ARBIN was utilized to realize the galvanostatic charge–discharge, cyclic voltammetry and EIS studies.

Results and discussion

Analysis of the phase and structure of BVONB synthesized at 15 min, BVONB/RGO-6, BVONB/RGO-12, and GO samples were performed. Fig. 2(a) shows the XRD pattern of the BVONB at 15 min that has characteristic peaks at 18°, 28.8°, 30.4°, 34.4°, 35°, 39.7°, 42.3°, 45.8°, 46.6°, 47.1°, 50.2°, 53.1°, 55.8°, 58.2°

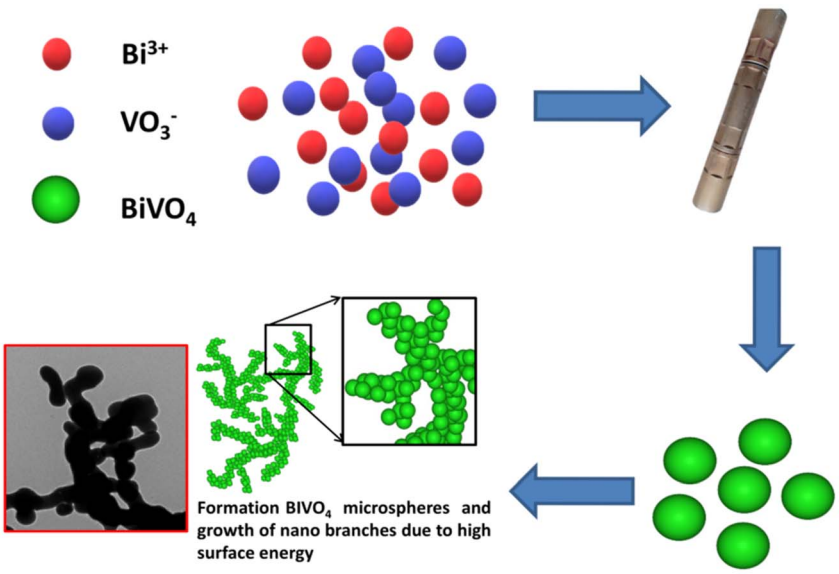

Fig. 1 Schematic illustration of the synthesis of the BVONB/RGO nanocomposite by SCW method synthesized at 400 °C for 15 min.

and 59.2° are assigned to (110), (011), (112), (004), (200), (002), (211), (150), (240), (042), (202), (161), (251), (321), and (123) crystal planes, respectively.[24] The clinobisvanite phase (PDF Card no.: 14-0688) was revealed with a monoclinic crystal structure including the space group *I*2/*b*. Fig. 2(b) also, shows the XRD pattern obtained for GO with a characteristic peak at 10.8°, assigned to the (001) crystal plane, which vanishes after SCW treatment, suggesting GO reduction to RGOs in BVONB/RGO nanocomposites. It is interesting to note that the intensity of the peaks decreases slightly with the increase of the RGO wt% in the nanocomposite, confirming the interruption to the continuous growth of the nano branches, thereby decreasing the intensity of the nanocomposite as observed in Fig. 2. As no impurity peaks were found further inferring the purity of the nanocomposite and single-phase BVONB formed.

The Raman spectra of BVONB, BVONB/RGO-6, and BVONB/RGO-12 are shown in Fig. 3(a–c). Fig. 3(a) shows a significant band at 811.6 cm^{-1} which is attributed to ν_s(V–O) representing the symmetric stretching of the VO_4 tetrahedron.[33] In Fig. 3(b and c) lattice peak G band at 1616 cm^{-1} corresponding to the sp^2 graphene lattice peak is seen clearly. Furthermore, the defect D band at 1352 cm^{-1} shows sp^3 disorder in the sp^2 lattice. The D and G band intensity ratio (I_D/I_G) will provide substantial information on the degree of disorder present in the carbon structure. The above said two prominent bands are not evident in pure BVONB. The spectral analysis of nanocomposites revealed the I_D/I_G values > 1, suggesting the reduction of GO to RGO in the SCW treatment.[34] Similar to XRD results, as the mass content of RGO increases the intensity of Raman bands at 811.6 cm^{-1} in BVONB/RGO nanocomposites decreases significantly, which is attributed to an increase in the RGO concentration.[22]

The morphologies of the synthesized BVONB and BVONB/RGO nanocomposites were characterized by SEM. The recorded images shown in Fig. 4 resemble 1D branched morphology.

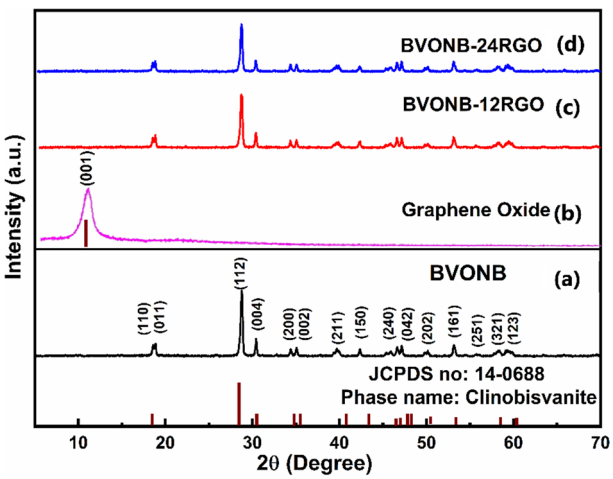

Fig. 2 XRD patterns of (a) BVONB 15 min, (b) GO sample synthesized by modified Hummer's method, (c) BVONB/RGO-6 and (d) BVONB/RGO-12 nanocomposite synthesized by SCW method synthesized at 400 °C for 15 min.

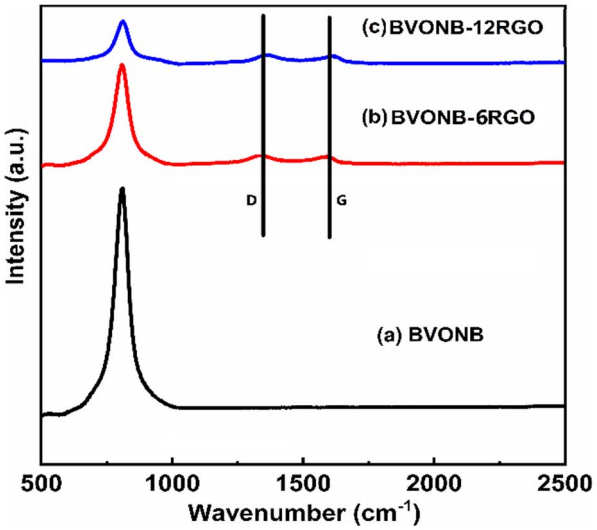

Fig. 3 Raman Spectra of (a) BVONB, (b) BVONB/RGO-6, and (c) BVONB/RGO-12 nanocomposite synthesized by SCW method synthesized at 400 °C for 15 min.

The SEM images (Fig. 4(b and c)) also depict the formation of BVONB and very well-dispersed RGO nanosheets forming the composite. The presence of RGO nanosheets in the images is visible and conclusive. Furthermore, in (Fig. 4(d–f)) TEM images infer sheet structures for pure BVONB as well as BVONB/RGO composites. It should also be noted that the formation of nano branches was due to the formation of smaller nanosized spherical particles. Furthermore, the TEM image Fig. 4(d) shows the good crystalline formation of BVONB growth ranging from nano to micrometer. The images substantiate the of formation BVONB/RGO nanocomposites and well-interspersed RGO nanosheets along with BVONB. It is also clearly visible from TEM images that with no restrictions to the growth of branches the sizes of BVONB are larger in growth. However, when GO was included the reduced growth is evident by the formation of inconsistent growth of branches as per Fig. 4(f). Fig. 4(g) shows the energy dispersive spectrum analysis (EDS) of $BiVO_4$-RGO12 confirming the presence of Bi, V, O, and C atoms to validate the presence of elements in the samples.

Fig. 5(a–d) provides an understanding of the valence states and composition of the surface elements, and the XPS spectrum analysis of the BVONB/RGO-24 nanocomposite. It can be seen from Fig. 5(a) that the survey spectra of the BVONB/RGO composite contain peaks related to C 1s, O 1s, Bi 4f, and V 2p. This substantiates the presence all four elements in the sample. Furthermore, the presence of trivalent Bi^{3+} oxidation states in the samples is also indicated by two characteristic binding energy peaks at 159.13 and 164.4 eV corresponding to Bi $4f_{7/2}$ and Bi $4f_{5/2}$ in Fig. 5(b). Also, in Fig. 5(c), the binding energies at 516.7 and 524.3 eV correspond to V $2p_{3/2}$ and V $2p_{1/2}$, respectively, indicating the presence of Vi^{5+} in the samples as prepared.[35] The peaks at 284.6, 285, and 286.9 eV correspond to sp^2 (C=C) hybridization, (C–O) hydroxyl, and (O=C–O) carboxyl, respectively as depicted in Fig. 5(d).[36] Inferring the

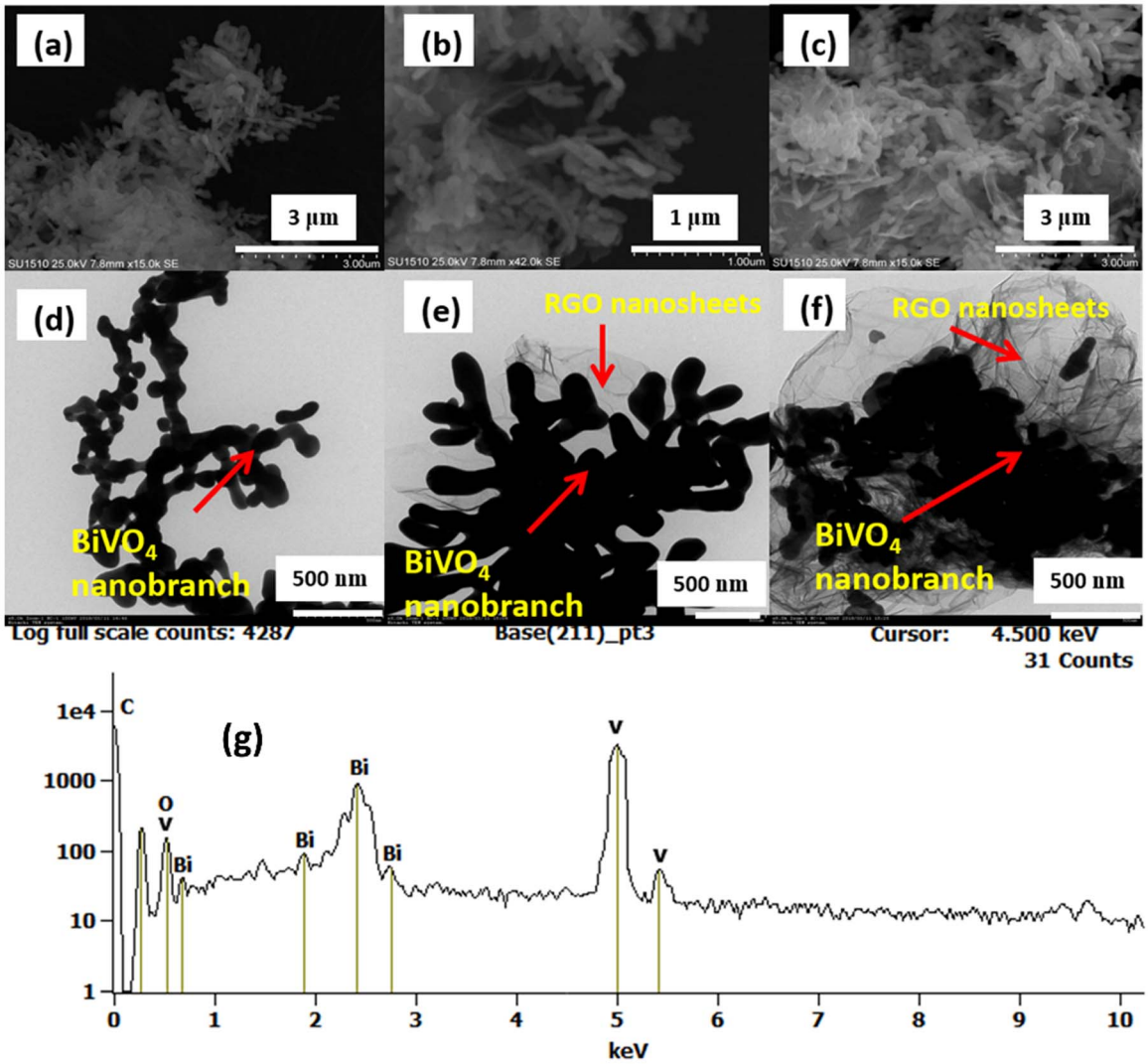

Fig. 4 SEM images of (a) BVONB 15 min, (b) BVONB/RGO-6, (c) BVONB/RGO-12, and TEM images of (d) BVONB 15 min, (e) BVONB/RGO-6, (f) BVONB/RGO-12 (g) EDS of BVONB/RGO-12 synthesized by SCW method synthesized at 400 °C for 15 min.

conversion of GO to RGO after SCW treatment, the intensity of C–O is low.

The thermal stability and RGO wt% of BVONB/RGO-24 nanocomposite, TGA analysis was performed and the results are shown in Fig. 6. For comparison, BVONB, BVONB/RGO-12, and BVONB/RGO-24 were analyzed between heating ranges of 50 to 800 °C at a heating rate of 10 min^{-1}. A steady fall in the mass detected at 200 °C in both samples can be attributed to the chemisorbed water molecules in sample.[37] Both BVONB/RGO-6 and BVONB/RGO-12 nanocomposite samples show a steep drop in weight between 200 to 500 °C that can be attributed to the loss of oxygen-containing functional groups and decomposition of carbon framework at higher temperatures.[38] From Fig. 6(b) and (c) the weight loss in BVONB/RGO-12 and BVONB/RGO-24 nanocomposite is calculated to be 3.2 and 4.2 wt% of nanocomposite samples, respectively.

The results of BVONB, BVONB/RGO-6, BVONB/RGO-12 nanocomposites, and GO characterized by FTIR spectroscopy are presented in Fig. 7(a–d). All samples show a typical absorption band at 3374 cm^{-1}. This band corresponds to the intercalated water, carboxyl, and OH groups.[36] The presence of a large number of oxygen-containing functional groups is evident from the FTIR spectrum of GO in Fig. 7(d). The stretching vibration of the C–O–C is represented by a prominent absorption peak at 1040 cm^{-1}. The peak at 1340 cm^{-1} corresponds to the bending of the carboxyl group (C–OH). The C=C stretching vibration causes an absorption peak at 1600 cm^{-1}. The stretching vibration of the carboxyl (C=O) is represented by a band at 1741 cm^{-1}. The presence of the carboxyl group on GO is suggested by the coexistence of two stretching modes, namely C=O and OH.[22] Furthermore, in Fig. 7(a–c), a strong peak in the band at 619 and 808 cm^{-1} can be attributed to Bi–O and VO_4^{3-}, respectively. The effective reduction of GO to RGO in BVONB/RGO nanocomposites can be deduced from the absorption band at 1741 cm^{-1}, which can only be observed in the GO sample.[22]

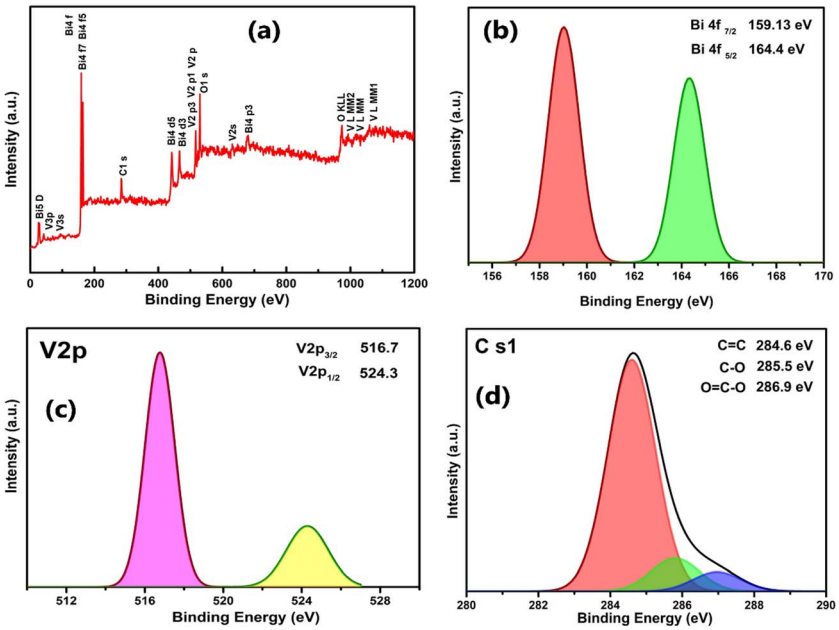

Fig. 5 XPS survey spectra of (a) BVONB/RGO-12 nanocomposite, (b) XPS spectra of Bi 4f, (c) XPS spectra of V 2p, (d) XPS spectra of C 1s, from BVONB/RGO-12 nanocomposite synthesized by SCW method synthesized at 400 °C for 15 min.

The illustration in Fig. 8 shows the formation of the BVONB/RGO composite. At first, the hydrolysis formed the Bi^{3+} ions, VO_4^{3+} ions from $Bi(NO_3)_3 \cdot 5H_2O$, and NH_4VO_3. The graphene oxide (GO) absorbed the Bi^{3+} ions due to the electrostatic attraction of negatively charged oxygen functional groups on its surface. During supercritical water treatment, the precursor solution has undergone hydrolysis and blending of Bi^{3+} ions and VO_4^{3+} ions. This formation of Bi_2O_3 resulted in a decrease of Bi^{3+} ions. This reduced reaction pace has resulted in the splitting of the nucleation and growth phase.[39] Now the nucleation begins when V_2O_5 aligns its growth along with Bi_2O_3 resulting in the formation of BVONP. As we understand from previous reports at SCW conditions a rapid decrease in the dielectric constant of water results in spontaneous saturation instantaneous precipitation of BVO. Furthermore, these particles grow into branched structures due to the absence of a ripening phenomenon in supercritical conditions. The nucleated seed prefers to grow into several 1D structures forming smaller branch-like structures and causing a reduction in surface energy. As the formed nanobranches aggregate to

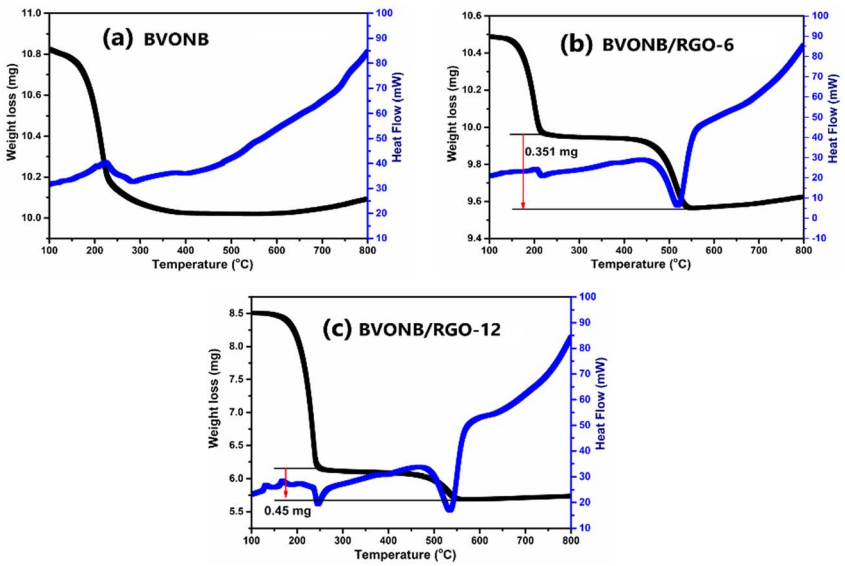

Fig. 6 TGA analysis of (a) BWS, (b) BVONB/RGO-6, and (c) BVONB/RGO-12 nanocomposites synthesized by SCW method synthesized at 400 °C for 15 min.

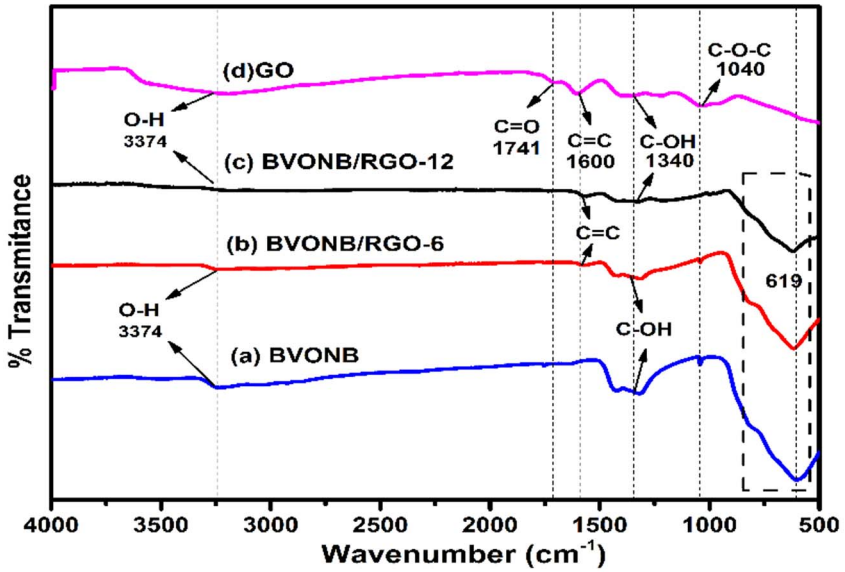

Fig. 7 FTIR analysis of (a) BVONB, (b) BVONB/RGO-6, (c) BVONB/RGO-12 nanocomposites synthesized by SCW method synthesized at 400 °C for 15 min and (d) GO by hummers method.

form into macro branches by continuous growth. Parallelly, the thermal reduction of GO to RGO is inferred under SCW treatment and is inferred by Raman spectroscopy.[34]

Electrochemical studies

Fig. 9(a–f) shows the storage behavior of Li^+ ions during the charging–discharging cycles. The voltammetric studies are shown in Fig. 9(a) at a scan rate of 0.1 mV. The peaks marked as R1, R2, R3 and R4 at 1.6 V, 1 V, 0.71 V, and 0.58 V confirm the reduction of Bi^{3+}, V^{5+} along with the formation of Li_2O forming the Secondary electrolyte interface layer.[40] The anodic peaks during charging depicted O1, O2, and O3 at 0.9 V and 1.3 V iterates the dealloying of Bi^+ and Li^+, respectively. Along with this an additional peak at 2.7 V is related to the Bi oxidation.[30] Further, the storage performance was assessed through galvanostatic charge–discharge measurements for the synthesized samples within the voltage range of 0 to 2.9 V at a rate of 0.1C. The Fig. 9(b) shows the CV curves at different scan rates from 0.1 mV s^{-1} to 1 mV s^{-1}. It can be seen that the scan rate increase is leading to higher polarization, which is indicated by the increased separation between the reduction and oxidation peaks. Furthermore, at 1 mV s^{-1}, the reduction and oxidation peaks can be identified, which infers fast-redox kinetics in the proposed electrochemical cell. The capacitive effects during

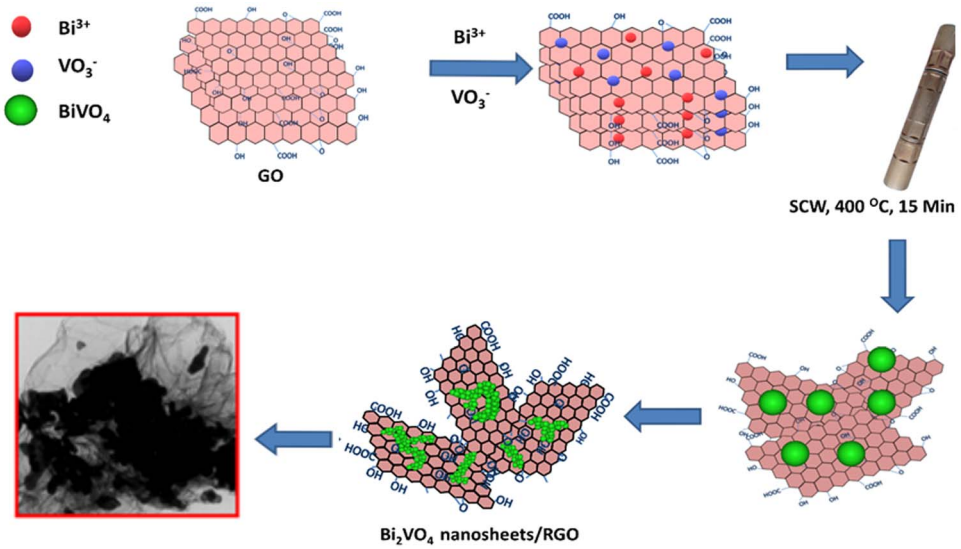

Fig. 8 Schematic illustration of the possible reaction mechanism for the formation of BVONB/RGO nanocomposite by SCW method at 400 °C for 15 min.

intercalation have been identified at different sweep rates and the relationship between scan rate (ν) and current (i) is defined using:

$$i = a\nu^b$$

b value is determined using the slope of $\log(\nu)$ *vs.* $\log(i)$ plot. Further, the b value indicates diffusion diffusion-dominated process if the slope is 0.5 and the slope is above 1 it infers the capacitive process. The slope value of 0.93 indicates a combination of diffusion and capacitance in the delithiation process.[41] As depicted in Fig. 9(c–f), the initial discharge capacities for BVONB, BVONB/RGO-6, BVONB/RGO-12, and BVONB/RGO-24 are approximately 810, 670, 750, and 750 mA h g^{-1}, respectively. However, as shown in Fig. 9(c), the reversible specific capacity of the pure BVONB sample

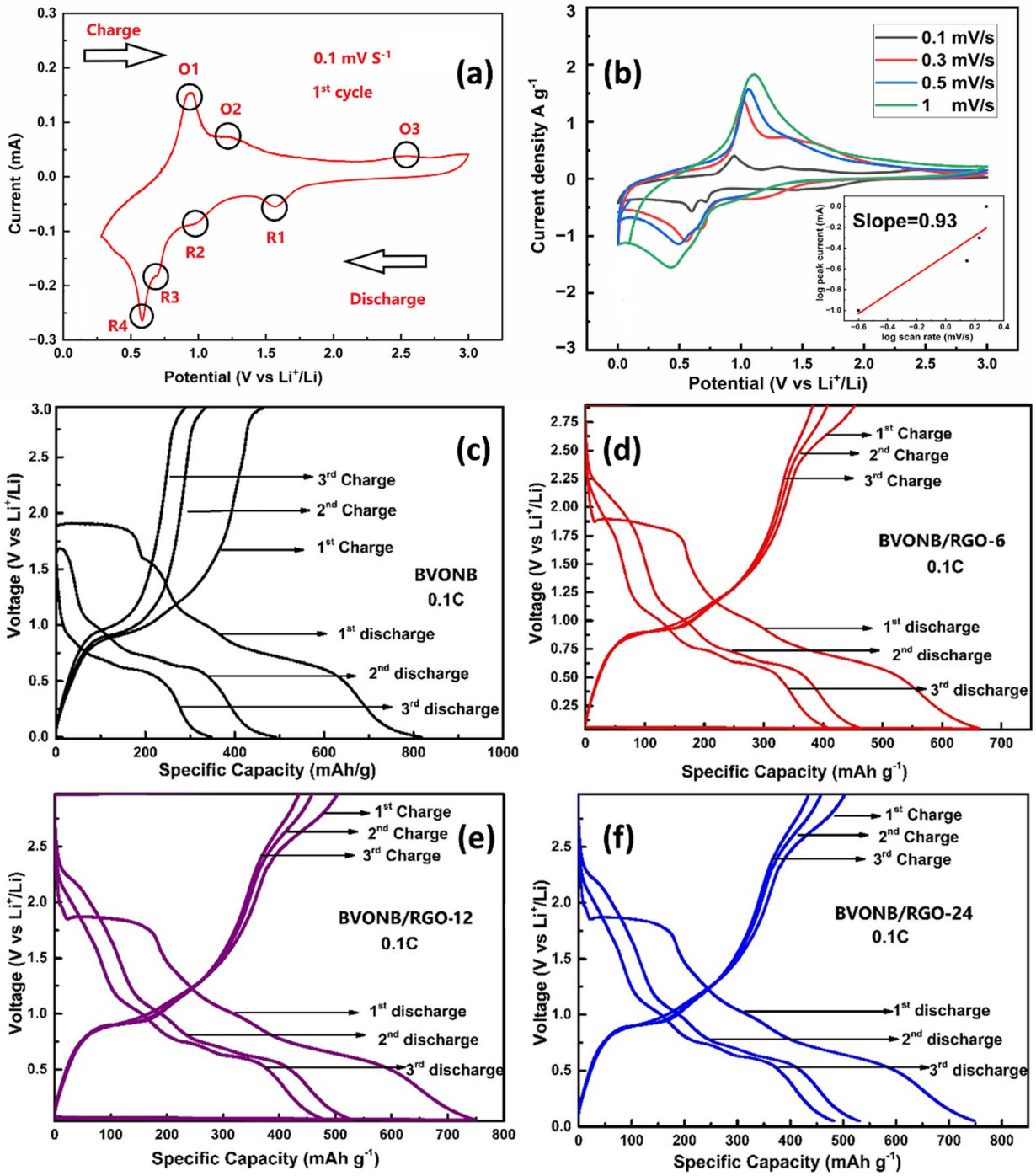

Fig. 9 (a) Cyclic voltammetry curve for BVONB. (b) Cyclic voltammetry curve for BVONB at different scan rates. Galvanostatic charge–discharge curves of (c) BVONB, (d) BVONB/RGO-6, (e) BVONB/RGO-12, (f) BVONB/RGO-24 nanocomposite anodes at 0.1C current density.

diminishes progressively during subsequent discharge cycles. This decline in specific capacitance is attributed to the formation of an irreversible solid electrolyte interface (SEI) and structural instabilities in the metal oxides during the processes of lithiation and de-lithiation. To address this issue, reduced graphene oxide (RGO) was employed as a conductive layer to facilitate the rapid diffusion of Li^+ ions and enhance the structural stability of the BVONB anode. Extended cycling tests indicate that the BVONB/RGO-12 sample displayed improved performance, suggesting that this composition represents the optimized nanocomposite with RGO. The expected responses during the charge/discharge cycles align with previously reported findings.[42,43]

Reversible Cycles:

$$3Li^+ + BiVO_4 + 3e^- \leftrightarrow Bi + Li_3VO_4 \quad (1)$$

$$3Li^+ + Bi + 3e^- \leftrightarrow Li_3Bi \quad (2)$$

Overall reaction:

$$BiVO_4 + 3Li^+ + 3e^- \leftrightarrow Li_3Bi + Li_3VO_4 \quad (3)$$

The galvanostatic discharge capacities of BVONB in the 3rd and 5th cycles were measured at 500 and 350 mA h g^{-1}, respectively. In contrast, BVONB/RGO-12 exhibited enhanced 2nd and 3rd discharge capacities of 530 and 480 mA h g^{-1}, respectively. This gradual decline in specific capacities can also be attributed to the incomplete decomposition of Li_2O in the solid electrolyte interface (SEI) layer, a common factor contributing to the decrease in specific capacities of metal oxide anodes.

It's important to note, as per eqn (1) and (2), that during reversible reactions, as the voltage reaches 3 V, various nanophases are formed in the electrode, including $LiVO_4$ and Li_3Bi. These nanoparticles play a significant role in storing Li^+ ions during the charging process in half-cells. RGO, being a conductive material, facilitates the movement of Li^+ ions across the electrode surface and into it by providing a conductive substrate for the dispersed Bi-metal atoms. Additionally, during lithiation/delithiation, the mechanical support offered by RGO helps mitigate the stress resulting from volume expansion in the layered BVONB structure during the formation of Bi, Li_3Bi, and Li_3VO_4. This is a primary factor contributing to the improved cycling performance of the BVONB/RGO-12-based anode.

The cyclic performance data in Fig. 10(a) reveal the performance of both pure BVONB and the BVONB/RGO nanocomposite anodes. It's evident that pure BVONB, along with BVONB/RGO-6, BVONB/RGO-12, and BVONB/RGO-24, does not exhibit long-term stability over 50 cycles, despite initially having higher discharge capacities. However, the sustained capacities achieved by VONB/RGO-12 over 50 cycles suggest a synergistic effect between RGO sheets and BVONB during cycling. Additionally, when the RGO content is increased to 12 wt%, the capacity decline becomes more pronounced as the BVO loading in the nanocomposite decreases. Fig. 10(b) coulombic efficiency of BVONB-based electrodes is seen to be around 56% in the first cycle which increased subsequently above 90% around the 10th cycle. The decrease in discharge capacity after 2nd cycle indicates the gradual formation by SEI layer formation. But, the coulombic efficiency is seen to be reaching 95% by the end of the 50th cycle. For the samples BVO with RGO composites the coulombic efficiency initially was found to be around 70% reaching 99% by 50th cycle. It is interesting to note that BVONB-based electrodes show variation in the coulombic efficiency, this can be attributed to constant volumetric expansion and pulverization of the electrodes in subsequent cycles. In contrast, the BVO-RGO-based electrodes show an increase in stability due to the synergetic effect of RGO providing conductivity for the movement of ions as well as mechanical stability to the structure avoiding the dissolution of the electrode into electrolyte. The EIS spectroscopy data of the sample depicted in Fig. 10(c) consisted of semicircles at the high-frequency range and sloping lines at low-frequency ranges. The real axis intercept at the beginning of the semicircle depicts a very low solution resistance (R_1). Further, the diameter of the semicircles for all the plots shows the charge transfer resistance (R_2) of the reaction. It can noted that the charge transfer resistance of pure BVONB around 700 Ω is much higher compared to BVO-RGO nanocomposites which are around 650, 600, and 300 Ω respectively. This can be related to the increase in weights of RGO in the nanocomposite samples providing better conductivity by providing channels for Li^+ diffusion.[44]

The rate capability test results shown in Fig. 10(d) inferred the superiority of BVONB/RGO-12-based anodes under different rates and their stability in comparison to other counterparts. BVONB/RGO-12 had a great reversible capacity at different C-rates from 0.1C–1C. Further, when retraced to 0.1C it was found that BVO-12RGO still delivered a capacity of nearly 270 mA h g^{-1}. It is also interesting to note that BVONB/RGO-24 also delivered a similar rate capability, but during cycling, it could not deliver the efficiency of BVONB/RGO-12. Even though graphite-based anode material can deliver 372 mA h g^{-1}, but, $BiVO_4$ based anodes with their higher theoretical specific capacity of 489 mA h g^{-1}, moreover provides the flexibility in optimization of morphology and particle size that can be utilized in gaining higher capacities. Furthermore, increasing the conductivity of nanoparticles by efficient carbon coating strategies will result in enhanced capacities but also provide large buffer volumetric changes during charging and discharging. The results demonstrate the superiority of BVONB/RGO-12-based anodes at various current rates and their overall stability compared to other counterparts. Considering the above capacity and cyclic stability of BVONB and its RGO nanocomposites has to be improved further. But overall as a process, it is very promising that the SCW synthesis technique can provide a processing technique that can be scaled up for large-scale production of MMOs.

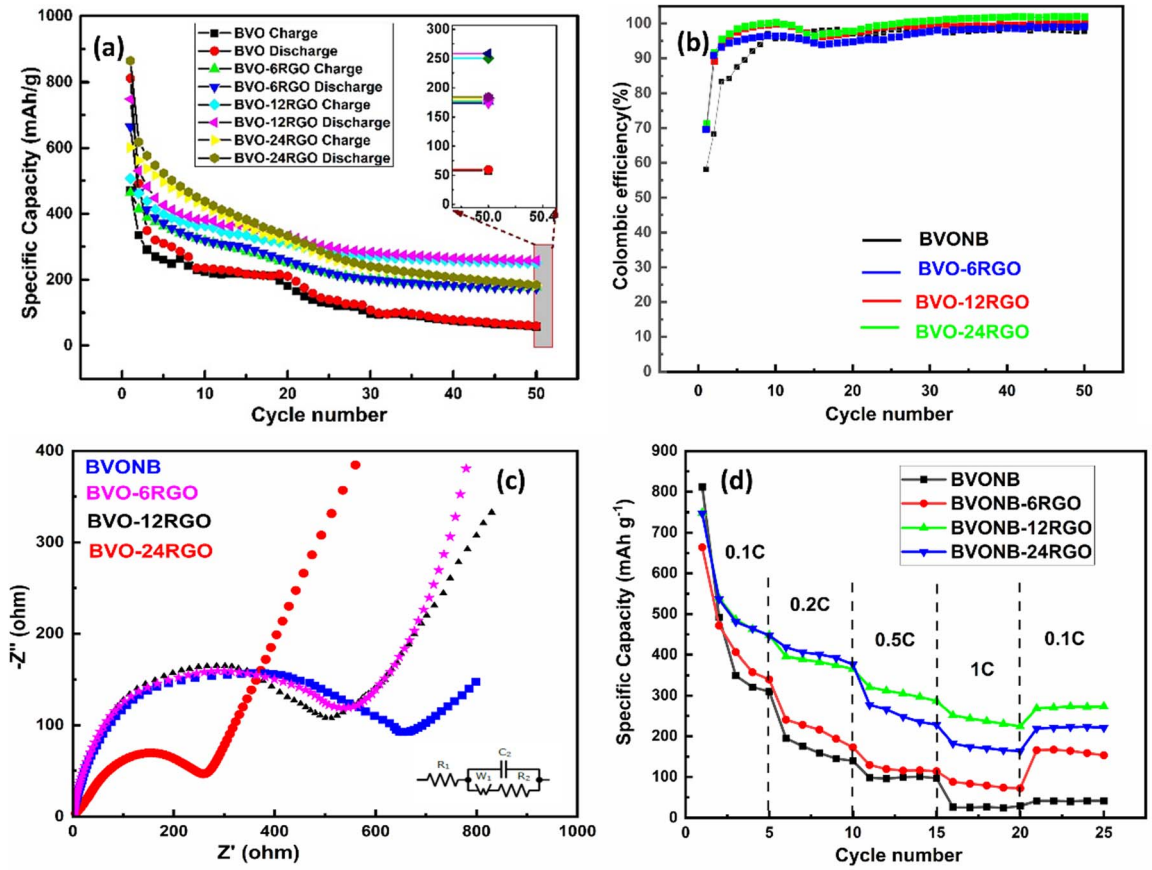

Fig. 10 (a) Cyclic test (b) coulombic efficiency plot (c) EIS study (d) rate capability tests at different C-rates for BVONB and its RGO nanocomposite anodes.

Conclusion

In summary, the synthesis of BVO and BVONB/RGO nanocomposites through the supercritical water method has proven to be a dependable one-pot approach for producing inorganic nanoparticles. Notably, the BVONB/RGO-12 nanocomposite exhibited an impressive initial discharge capacity of up to 750 mA h g^{-1} and maintained a stable specific capacity of 260 mA h g^{-1} even after 50 cycles. This stable performance is attributed addition to the synergetic effect of RGO and, further, strategies like change in morphology of BVO nanoparticles and better carbon coating to facilitate the movement of Li^{+} ions by interconnecting and reducing the path of travel can result in a substantial increase of cycle life. Additionally, the SCW one-pot synthesis technique stands out as a reliable and scalable method for creating RGO-based nanocomposites. Collectively, these findings indicate the promising potential of BVO-RGO nanocomposites as cost-effective Li-ion battery electrode materials, with substantial room for enhancement in their rate capability for Li-ion storage applications.

Author contributions

Dinesh Rangappa and Manjunath Shetty conceived and designed the work and performed experiments. Karnan Manickavasakam and Manikandan Kandasamy carried out the electrochemical experiments. Chandrakantha Bekal conducted XRD and SEM analysis. Izan Izwan Misnon conducted the XPS analysis, and Murthy Muniyappa conducted the FTIR and TGA analysis. Satish Shenoy B prepared the final draft of the paper; all the authors participated in the analysis and discussion of the results.

Conflicts of interest

There are no conflicts to declare.

Acknowledgements

The authors would like to thank the Manipal Institute of Technology, Manipal Academy of Higher Education, for the Internal seed money Grant (Seed money id: 00000708).

References

1 D. Choi, N. Shamim, A. Crawford, Q. Huang, C. K. Vartanian, V. V. Viswanathan, M. D. Paiss, M. J. E. Alam, D. M. Reed and V. L. Sprenkle, *J. Power Sources*, 2021, **511**, 230419.

2 S. Verma, B. Padha, S. J. Young, Y. L. Chu, R. Bhardwaj, R. K. Mishra and S. Arya, *Prog. Solid State Chem.*, 2023, **72**, 100425.
3 V. Etacheri, R. Marom, R. Elazari, G. Salitra and D. Aurbach, *Energy Environ. Sci.*, 2011, **4**, 3243–3262.
4 B. Padha, S. Verma, Prerna, A. Ahmed, S. P. Patole and S. Arya, *Appl. Energy*, 2024, **356**, 122402.
5 P. Mahajan, S. Verma, B. Padha, A. Ahmed and S. Arya, *J. Alloys Compd.*, 2023, **968**, 171904.
6 K. Edström, M. Herstedt and D. P. Abraham, *J. Power Sources*, 2006, **153**, 380–384.
7 C. Fang, X. Wang and Y. S. Meng, *Trends Chem.*, 2019, **1**, 152–158.
8 S. Mahmud, M. Rahman, M. Kamruzzaman, M. O. Ali, M. S. A. Emon, H. Khatun and M. R. Ali, *Results Eng.*, 2022, **15**, 100472.
9 Y. Zhao, X. Li, B. Yan, D. Xiong, D. Li, S. Lawes and X. L. Sun, *Adv. Energy Mater.*, 2016, **6**, 1502175.
10 A. Ahmed, S. Verma, P. Mahajan, A. K. Sundramoorthy and S. Arya, *Sci. Rep.*, 2023, **13**(1), 1–12.
11 D. Jiao, Z. Xie, Q. Wan and M. Qu, *J. Energy Chem.*, 2019, **37**, 73–81.
12 X. Cai, L. Lai, Z. Shen and J. Lin, *J. Mater. Chem. A*, 2017, **5**, 15423–15446.
13 P. Liu, K. Zhu, K. Bian, Y. Xu, F. Zhang, W. Zhang, J. Zhang and W. Huang, *J. Alloys Compd.*, 2018, **765**, 901–906.
14 A. Bhaskar, M. Deepa, T. N. Rao and U. V. Varadaraju, *J. Power Sources*, 2012, **216**, 169–178.
15 C. Te Hsieh, J. Y. Lin and C. Y. Mo, *Electrochim. Acta*, 2011, **58**, 119–124.
16 M. B. Vazquez-Santos, P. Tartaj, E. Morales and J. M. Amarilla, *Chem. Rec.*, 2018, **18**, 1178–1191.
17 X. Wang, L. Qiao, X. Sun, X. Li, D. Hu, Q. Zhang and D. He, *J. Mater. Chem. A*, 2013, **1**, 4173–4176.
18 L. Fan, W. Zhang, S. Zhu and Y. Lu, *Ind. Eng. Chem. Res.*, 2017, **56**, 2046–2053.
19 J. Jiang, Y. Li, J. Liu, X. Huang, C. Yuan, X. Wen Lou, J. Jiang, J. P. Liu, X. T. Huang, Y. Y. Li, C. Z. Yuan and X. W. Lou, *Adv. Mater.*, 2012, **24**, 5166–5180.
20 L. Hu, X. Chen and C. Feng, *Ionics*, 2022, **28**, 1483–1493.
21 M. Shetty, M. Murthy, M. Shastri, M. Sindhusree, H. P. Nagaswarupa, P. D. Shivaramu and D. Rangappa, *Ceram. Int.*, 2019, **45**, 24965–24970.
22 M. Shetty, C. Schüßler, M. Shastri, C. Sabbanahalli, C. P. Chitrabhanu, M. Murthy, S. Jagadeesh Babu, T. Tomai, K. S. Anantharaju, P. D. Shivaramu and D. Rangappa, *Ceram. Int.*, 2021, **47**, 10274–10283.
23 H. Qian, Y. Liu, H. Chen, K. Feng, K. Jia, K. Pan, G. Wang, T. Huang, X. Pang and Q. Zhang, *Energy Storage Mater.*, 2023, **58**, 232–270.
24 D. P. Dubal, D. R. Patil, S. S. Patil, N. R. Munirathnam and P. Gomez-Romero, *ChemSusChem*, 2017, **10**, 4163–4169.
25 S. Verma, P. Mahajan, B. Padha, A. Ahmed and S. Arya, *Electrochim. Acta*, 2023, **465**, 142933.
26 G. L. Li, *RSC Adv.*, 2017, **7**, 9130–9140.
27 D. P. Dubal, K. Jayaramulu, R. Zboril, R. A. Fischer and P. Gomez-Romero, *J. Mater. Chem. A*, 2018, **6**, 6096–6106.
28 R. Xie, Y. Li, H. Huang, L. Su, L. Li, X. Pan, Z. Guo, F. Luo, Z. Guo, B. Guo, F. Chi, Y. Ma and H. Liu, *Ceram. Int.*, 2020, **46**, 3119–3123.
29 D. R. Patil, S. D. Jadhav, A. Mungale, A. S. Kalekar and D. P. Dubal, *Mater. Lett.*, 2019, **252**, 235–238.
30 D. Fang, M. Cui, R. Bao, J. Yi and Z. Luo, *Solid State Ionics*, 2020, **346**, 115222.
31 T. Adschiri and A. Yoko, *J. Supercrit. Fluids*, 2018, **134**, 167–175.
32 D. C. Marcano, D. V. Kosynkin, J. M. Berlin, A. Sinitskii, Z. Sun, A. Slesarev, L. B. Alemany, W. Lu and J. M. Tour, *ACS Nano*, 2010, **4**, 4806–4814.
33 A. P. Nowak, K. Trzciński, M. Szkoda, J. Karczewski, M. Gazda and A. Lisowska-Oleksiak, *Synth. Met.*, 2019, **257**, 116168.
34 V. Scardaci and G. Compagnini, *C*, 2021, **7**, 48.
35 S. S. Mali, G. R. Park, H. Kim, H. H. Kim, J. V. Patil and C. K. Hong, *Nanoscale Adv.*, 2019, **1**, 799–806.
36 M. Shetty, K. Manickavasakam, C. Sabbanahalli, C. Bekal, I. I. Misnon, A. P. Subrahmanya, K. Roy, P. D. Shivaramu, S. B. Shenoy and D. Rangappa, *J. Energy Storage*, 2023, **72**, 108116.
37 A. Bekhoukh, I. Moulefera, L. Sabantina and B. Abdelghani, *Polymers*, 2021, **13**, 3344.
38 L. Huang, P. Zhu, G. Li, D. Lu, R. Sun and C. Wong, *J. Mater. Chem. A*, 2014, **2**, 18246–18255.
39 S. Yuan, Y. Zhao, W. Chen, C. Wu, X. Wang, L. Zhang and Q. Wang, *ACS Appl. Mater. Interfaces*, 2017, **9**, 21781–21790.
40 H. Liu, X. Shi, L. Zhang, X. Shi and J. Zhang, *Ionics*, 2022, **28**, 689–696.
41 K. Li, J. Zhang, D. Lin, D. W. Wang, B. Li, W. Lv, S. Sun, Y. B. He, F. Kang, Q. H. Yang, L. Zhou and T. Y. Zhang, *Nat. Commun.*, 2019, **10**, 1–10.
42 Q. Wang, Z. Chen, S. Bai, X. Wang and Y. Zhang, *J. Alloys Compd.*, 2023, **958**, 170485.
43 D. P. Dubal, K. Jayaramulu, R. Zboril, R. A. Fischer and P. Gomez-Romero, *J. Mater. Chem. A*, 2018, **6**, 6096–6106.
44 Z. Chu, X. Zhao, Q. Wang, T. Bao, H. Li, Y. Cao, B. Zhang, J. Cao and W. Si, *Crystals*, 2023, **13**, 547.